Article

Not peer-reviewed version

Performance Evaluation of a Tunnel-Slope System Under Heavy Rain-Fall Conditions

Juan Manuel Mayoral *, Paola Martínez Castelán, Mauricio Peréz, Azucena Román de la Sancha *, Francisco Suarez Fino

Posted Date: 8 May 2026

doi: 10.20944/preprints202605.0471.v1

Keywords: performance; estimation of factor of safety and deformations; back-analysis; tunnel–slope interaction; numerical modelling

 doi:10.20944/preprints202605.0471.v1

Article

Performance Evaluation of a Tunnel-Slope System Under Heavy Rain-Fall Conditions

Juan Manuel Mayoral [1,*], Paola Martínez Castelán [1], Mauricio Peréz [1], Azucena Román de la Sancha [2,*] and Francisco Suarez Fino [1]

[1] Instituto de Ingenieria, Universidad Nacional Autónoma de México, Mexico City, Mexico

[2] School of Engineering and Sciences, Tecnológico de Monterrey, Monterrey, Mexico

* Correspondence: jmayoralv@iingen.unam.mx (J.M.M.); a.roman@tec.mx (A.R.d.l.S.)

Abstract

Intense rainfall, and the resulting increase in ground saturation can significantly modify the mechanical performance of rock masses in natural slopes. This is particularly important if material fractured is present. Extended infiltration accelerates material degradation, reduces shear strength along discontinuities, and increases pore-water pressures, reducing effective stresses, and in turn, raises the probability of large-scale landslides. Evaluating these processes requires a thorough understanding of the geotechnical and hydrogeological properties controlling slope response, as well as reliable stability assessments under varying saturation conditions, including factor of safety and deformation estimates. However, in engineering practice most of the time ground exploration is limited, and laboratory testing in rocks only provides an estimation of the rock performance expected in the slope within a reduced zone. This study examines a landslide triggered in a shale–limestone slope after heavy rainfall. A back-analysis was performed within a performance-based design (PBD) framework to reproduce the observed failure and, thus, characterize representative geomechanically parameters for design validation, using three-dimensional finite difference modeling. The performance under monotonic and seismic loading of a tunnel built adjacent to the slope was analyzed as a mitigation measure, thus establishing its technical soundness, from both state limit of failure and service, of the tunnel-slope system.

Keywords: performance; estimation of factor of safety and deformations; back-analysis; tunnel–slope interaction; numerical modelling

1. Introduction

Slope instability in fractured and weathered rock is often observed in cuts of highways and roads passing through hilly and mountain chain areas, especially during rainy season. This has been exacerbated by climate change, which have produced storm systems that may last several weeks, and in which the rain intensity in a short period of time can lead to floodings (Ferrario et. Al 2024). In practice, very often the rock strength parameter characterization relies upon the slope failures back analysis (Sarah et al. 2024), along with the Hooke and Brown approach. This method is based mostly in in-situ observation and point-specific measurements of unconfined rock strength and deformability parameters, which, considering in situ features such as fault orientation, and crack filling, allows assigning both strength and deformability parameters (Wu et. Al 2023). When the slope instability leads to road closing due to general failures, where significant volumes of debris is mobilized, a practice-oriented approach is to build a tunnel to bypass the unstable area. This, approach requires in-depth performance assessment evaluation of the slope-tunnel system under monotonic and seismic loading (Li, Z et al. 2023). However, currently, there is a lack of information in the technical literature regarding the complex interaction of tunnel-slope systems in rock, and the impact of this interaction its expected performance during heavy rainfall (Wei, H. 2025). This paper

 doi:10.20944/preprints202605.0471.v1

presents a case study in which the seismic performance of a slope-tunnel system in fracture rock subjected to heavy rainfall is evaluated.

1.1. Case Study

A landslide triggered by heavy rainfall blocked approximately 100 meters of a highway crossing a major mountain system in Mexico. The failed area is located within a formation composed of a sequence of shales, calcareous sandstones, argillaceous limestones with a "flyschoide" appearance, and laminar marls. The proportion of shales to sandstones varies depending on the particular zone. The sandstones are coarse- to medium-grained, poorly sorted, and cemented by a calcareous matrix. The shales are laminated, thin-bedded, and highly fractured. Clayey limestones are grey in color and have a compact, folded structure. Figure 1 shows an image of the main geological formation and the occurred landslide.

Figure 1. Main geological formation and landslide of the case study.

2. Methodology

A performance-based assessment of the tunnel–slope system was carried out following the methodology depicted in Figure 2. The process starts with field and geological characterization of the fault to identify the mechanisms controlling slope instability. Based on these observations, a back-analysis procedure was carried out to obtain preliminary geomechanical properties capable of reproducing the observed failure conditions. These properties were contrasted with those obtained from the Hoek–Brown, HB, failure criterion, and subsequently refined through numerical calibration. Once defined the calibrated parameters, some technically sound engineering solutions were proposed to mitigate the identified instability mechanisms. From all the alternatives, build a tunnel to bypass the unstable area was the chosen solution. Using calibrated properties, detailed three-dimensional numerical models were developed to simulate the tunnel excavation process, explicitly accounting for the fault zone, the surrounding ground conditions, and the structural support elements.

 doi:10.20944/preprints202605.0471.v1

The numerical results were subsequently used for the performance evaluation of the slope-tunnel system, focusing on stability, deformation control, and structural demand on the tunnel support system. Finally, once the tunnel construction was simulated, the seismic performance of the tunnel-slope system is assessed with the numerical model, and the stability is verified based on predefined performance objectives within the Performance-Based Design framework.

Figure 2. Flowchart of the method.

For the tunnel structure, the following criteria were adopted: Diametral strain ratio (ΔD/D): Used to evaluate cross-sectional distortion, with reference limits of 0.5% for tunnels in rock according to Eurocode 8, and axial force demand: Compared against the structural capacity of the lining to verify structural integrity.

3. Rock-Mass Characterization

The rock mass was classified using the Geological Strength Index (GSI), developed by Hoek & Brown (1997), based on field observations. It exhibited characteristics of a flysch-type formation, consisting of alternating medium to thick limestone layers and thin shale strata. From the GSI parameter, and other rock strength parameters, it is possible to estimate the failure envelope according to the generalized Hoek-Brown model, which is defined by the following equation:

$$\sigma_{cm} = \sigma'_3 + \sigma_{ci}(m_b \frac{\sigma'_3}{\sigma_{ci}} + s)^a \quad (1)$$

where σcm is the equivalent uniaxial compressive strength of the rock mass; σci is the uniaxial compressive strength of the intact rock; and $\sigma'3$ is the minor principal stress. Likewise, the values of a, m_b and s are determined with the following equations:

$$a = \frac{1}{2} + \frac{1}{6}(e^{\frac{GSI}{15}} - e^{-\frac{20}{3}}) \quad (2)$$

$$m_b = m_i e^{\frac{GSI-100}{28-14D}} \quad (3)$$

$$s = e^{\frac{GSI-100}{9-3D}} \quad (4)$$

 doi:10.20944/preprints202605.0471.v1

where GSI is the parameter that considers the structural characteristics of fracturing, the alteration state of the discontinuities, and the surface of the rock mass. In this case, a value of D = 0 is suggested when the excavation is carried out by mechanical or manual means for low-quality rocks, resulting in minimal impact on the surrounding rocks.

To define the uniaxial compressive strength of the intact rock, σci, the values from laboratory tests performed on rock cores extracted from the boreholes were used.

For calculations using numerical methods, a Mohr-Coulomb failure criterion was established to represent the behavior of the rock mass. Therefore, the cohesion (c), internal friction angle (∅), and Young's modulus (E_m) parameters of the rock mass were estimated. The strength envelope of the rock mass was established according to the Generalized Hoek & Brown constitutive model, and subsequently, the equivalent Mohr-Coulomb constitutive law was determined. The expressions used were as follows:

$$c = \frac{\sigma_{cm[(1+2a)s+(1-a)m_b\sigma'_{3n}](s+m_b\sigma'_{3n})^{a-1}}}{(1+a)(2+a)\sqrt{1+\frac{6am_b(s+m_b\sigma'_{3n})^{a-1}}{(1+a)(2+a)}}} \quad (5)$$

$$\emptyset = sin^{-1}\left[\frac{6am_b(s+m_b\sigma'_{3n})^{a-1}}{2(1+a)(2+a)+6am_b(s+m_b\sigma'_{3n})^{a-1}}\right] \quad (6)$$

$$E_m(GPa) = \left(1-\frac{D}{2}\right)\sqrt{\frac{\sigma_{ci}}{100}} * 10^{\lfloor\frac{GSI-10}{40}\rfloor} \quad (7)$$

where σ_cm is the uniaxial compressive strength of the intact rock. The value of 〖σ'〗_3n is determined with the following equation:

$$\sigma'_{3n} = \frac{\sigma'_{3max}}{\sigma_{cm}} \quad (8)$$

〖σ'〗_3max is the maximum value of the confinement effort that can occur at the site.

Table 1 shows the estimated Hoek-Brown parameters.

Table 1. Summary of parameters of the generalized Hoek & Brown constitutive model for geotechnical units.

Geotechnical Units	Unit	σci (MPa)	GSI	mi	D
Slope deposits	UG1	NA	NA	NA	NA
Highly weathered shales and limestones	UG2	38.5	15	7	0
Moderately weathered shales and limestones	UG3	65.6	25	7	0

Where σci is the single compressive strength parameter, GSI and D are rock strength parameters and mi is a constant that depends on the type of rock, and UG are the geotechnical units.

Based on this data, Morh-Coulomb equivalent parameters were stated (cohesion and friction angle), and Young's modulus was calculated as a function of the Geological Strength Index (GSI). Table 2 shows the initial parameters used in the analyses. Stratigraphy for analysis was developed from field surveys, in-situ tests, geophysical data, boreholes, and laboratory analyses to define layering and geomechanical properties. Three geotechnical units were identified (Table 2). Unit 1: Slope deposits, unit 2: Highly weathered shales and limestones and unit 3: Moderately weathered shales and limestones.

 doi:10.20944/preprints202605.0471.v1

Table 2. Initial geotechnical parameters used for the analysis.

Layer	γ (k/m3)	Em [MPa]	ν	C [kPa]	φ [°]
Slope deposits	20.0	100	0.35	30	35
Highly weathered shales and limestones	24.0	770	0.30	300	34
Moderately weathered shales and limestones	24.0	1850	0.30	300	40

Where γ is the unit weight of the material, Em the Young's modulus of the rock mass, ν the Poisson's ratio, C is the Cohesion, and ϕ the Friction angle.

Figure 3 shows the geological-geotechnical profile of the landslide, the stratigraphy, the identified failure surfaces, and possible location of the tunnel.

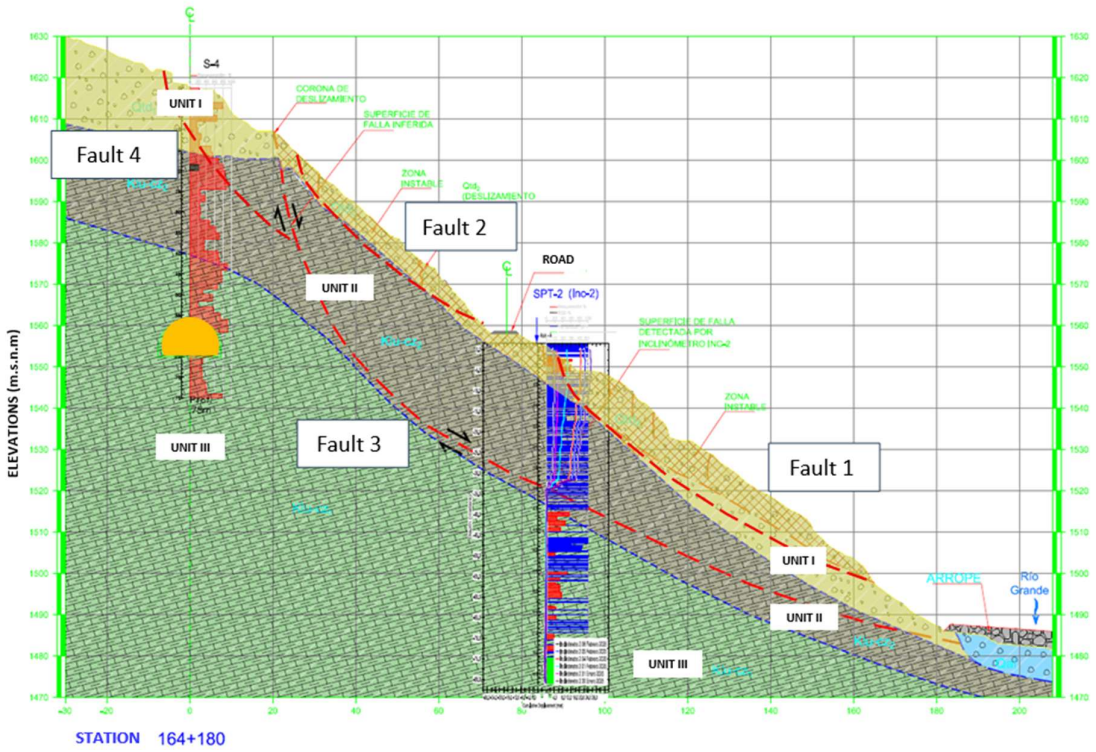

Figure 3. Geological-geotechnical profile of the case study.

4. Numerical Model

4.1. Limit Equilibrium Method

The SLIDE program, a specialized 2D limit equilibrium software for slope stability, was used initially to establish the failure of surface and factor of safety, with the limit equilibrium method. This program enables the evaluation of the factor of safety (FS), or the probability of failure of circular or non-circular slip surfaces on soil or rock slopes. Using various search and optimization algorithms, the analysis generates the minimum safety FS, which corresponds to the critical failure surface. This surface is then analyzed through discretization using the slice method. Sensitivity analyses can also be performed, in which resistance parameters are varied to determine their impact on the FS.

The inverse analysis, based on the limit equilibrium method, was performed using sensitivity analysis, the objective of which was to find the combinations of strength properties that resulted in a factor of safety (FS) ≈ 1. To carry out these analyses, a fixed friction angle was established, and the cohesion was varied within a specific range to obtain the cohesion vs. FS relationship. This analysis

 doi:10.20944/preprints202605.0471.v1

was repeated considering various friction angle values to obtain the cohesion and friction angle combinations that resulted in an FS ≈ 1. Circular and non-circular failures were considered, as well as dry and saturated conditions in the slope body.

Table 3 shows a summary of all the strength parameter combinations obtained for each of the analysis conditions.

Table 3. Summary of the parametric analyses to estimate the combinations of slope failure properties using the limit equilibrium method.

φ (°)	Fault cohesion (kPa)		
	Dry Circular	Dry No-Circular	Saturated
5	350	280	385
10	290	255	345
15	200	180	295
20	129	125	255
25	75	82	220
30	35	39	180

Once the possible combinations of strength parameters that could lead to slope failure were established, the analysis was performed considering the actual stratigraphy of the site. Figure 4 illustrates the graphical results of the stability analysis considering these properties. The critical failure surfaces are concentrated in the slope deposits, at the bottom and top of the slope.

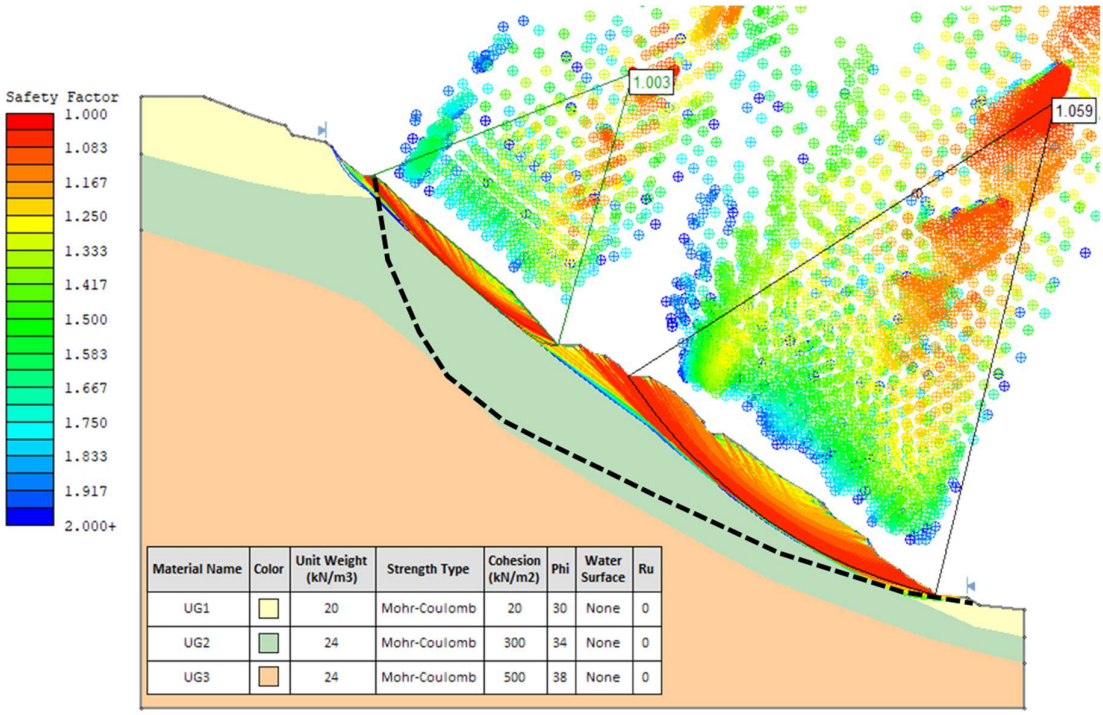

Figure 4. Local failure surfaces identified in the slope deposits.

4.2. Parametric Back Analyses Based on Observed Failure Surface

Back-analyses of the observed failure were conducted using the estimated strength and stiffness parameters, with sets of finite difference models, and the strength-reduction method. Stability

 doi:10.20944/preprints202605.0471.v1

analyses were performed to reproduce the observed failure surface of Figure 3, varying the cohesion, and maintaining friction angle constant, until achieving a safety factor SF≈1, considering both dry and saturated conditions. Figure 5 shows the finite difference mesh used for the slope assessed in FLAC3D. After performing several analyses, a summary graph was generated showing all possible combinations of parameters that could have caused the slope failure, both under dry and saturated conditions. Figure 6 shows this summary.

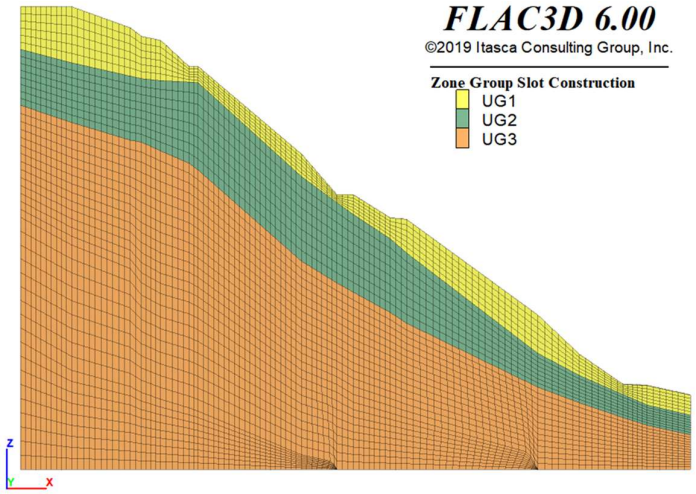

Figure 5. Finite difference mesh used in stability analysis.

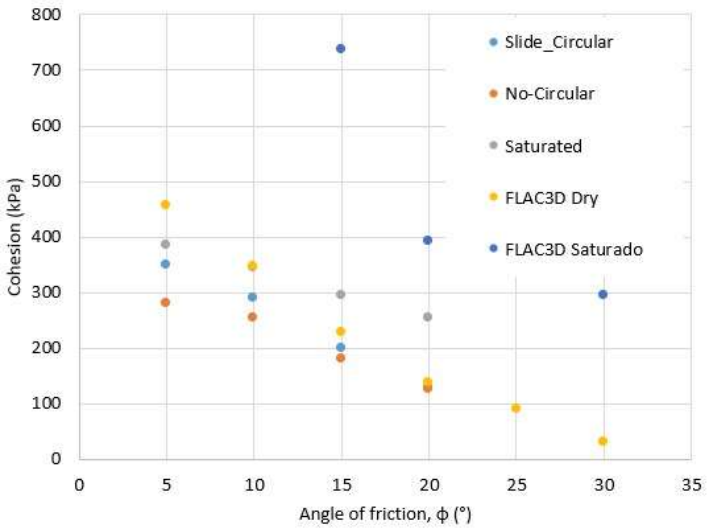

Figure 6. Summary of the parametric analyses performed with limit equilibrium and with parameter reduction.

Figure 7 presents the stability results with the cohesion-friction angle combination that reproduced the failure surface considering dry conditions. The failures developed were within the slope deposits at the toe and crest, with a failure cohesion of approximately 21 kPa. The predicted mechanisms agreed with field observations, where initial sliding occurred at the lower slope, followed by instability at the upper slope prior to global collapse.

 doi:10.20944/preprints202605.0471.v1

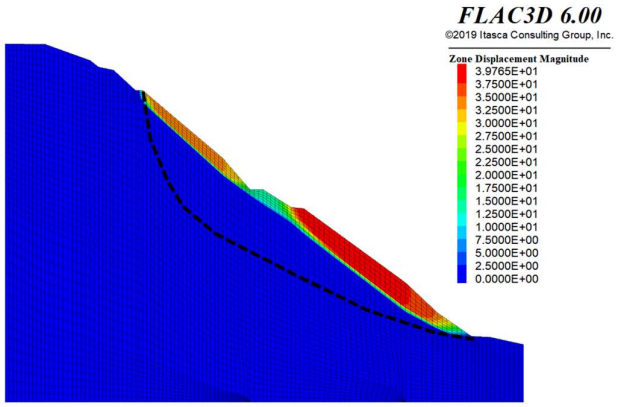

Figure 7. Slope displacement contours at the onset of failure in UG1. Units in [m].

The next step was to evaluate the stability of the slope assuming saturated conditions due to the rainy season. Figure 8 presents the displacement contours where it can be appreciated that the failure mechanism calculated with the model, reproduce adequately the estimated failure with field observations. The results indicated a failure cohesion of approximately 154 kPa for Geotechnical Unit 2.

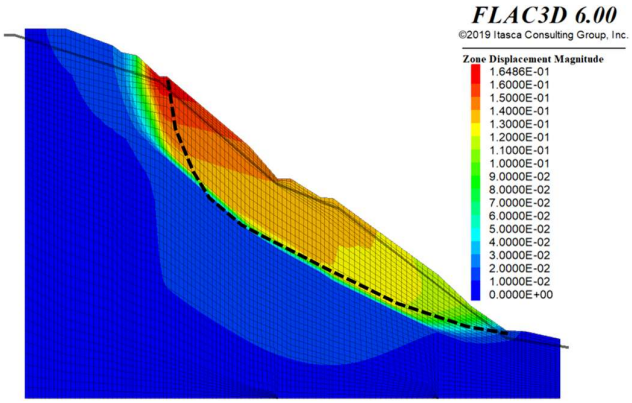

Figure 8. Displacement contours on the slope, when the fault occurs in UG2, under saturated conditions. Units in [m].

The comparison between field data and back-analysis results showed that the global failure occurred during the rainy season, which correspond to saturated conditions with FS≈1, consistent with a critical stability state. In contrast, dry conditions reproduced adequately the shallow failures, which occurred progressively. Phicometer tests were carried out at roadway level, to verify the values of the proposed parameters, and good fit was found. The calibrated parameters adopted for tunnel simulation are summarized in Table 4.

Table 4. Calibrated geotechnical parameters used for the numerical analyses.

Unit	γ (k/m3)	Em [MPa]	ν	Cohesion [kPa]	φ [°]
Slope deposits	20.0	100	0.35	25	30
Highly weathered shales and limestones (unaltered)	24.0	800	0.30	155	34
Highly weathered shales and limestones (residual)	24.0	790	0.30	46	30
Moderately weathered shales and limestones	24.0	1410	0.30	167	40

 doi:10.20944/preprints202605.0471.v1

4.3. Tunneling Process Simulation

A road tunnel was proposed as a mitigation measure, located at 4 tunnel diameters from the slope to avoid interaction between the tunnel and the slope. The proposed tunnel has a total length of 393.6 m, a width of 15.8 m, and a height of 9.5 m, with 355 m to be excavated. Construction will proceed in three alternating excavation–support cycles with a maximum advance of 2 m, using steel frames, shotcrete, and umbrella pipes, as tunnel support.

A three-dimensional numerical model was developed to assess ground stability and the performance of the proposed support system during tunnel excavation. Owing to the tunnel length, the model was divided into three sections: entrance portal, central section, and exit portal. Due to space restrictions only the results of the central section are included in this paper. Figure 9 illustrates the extent of each modeled section.

Figure 9 shows the construction stages considered in the tunnel section and Figure 10 shows the definition of the construction stages according to procedure ST1, in Figure 11 the procedure ST2 and in Figure 12 the definition of procedure ST3.

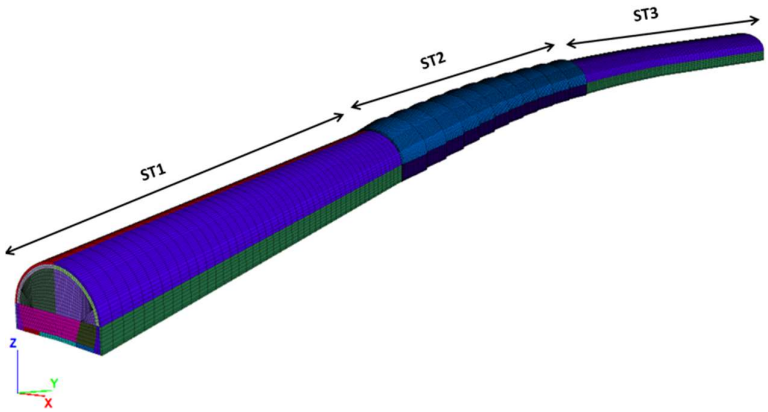

Figure 9. Definition of construction stages of the tunnel section.

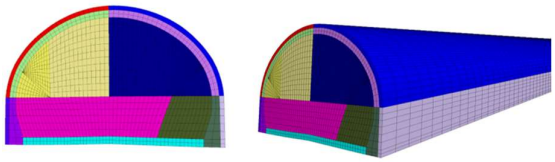

Figure 10. Definition of construction stages according to procedure ST1.

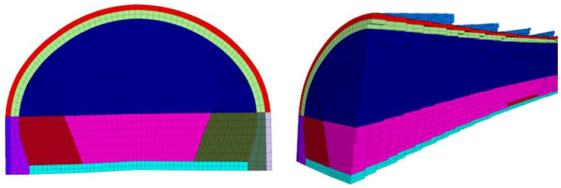

Figure 11. Definition of construction stages according to procedure ST2.

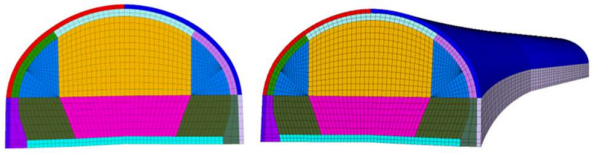

Figure 12. Definition of construction stages according to procedure ST3.

 doi:10.20944/preprints202605.0471.v1

For procedure ST1.

1. First stage: Sides of the upper half-section

The side sections are excavated in 3 m increments, compacting the soil and applying an initial layer of fibre-reinforced shotcrete to stabilize the vault.

2. Second stage: Right upper half-section

Excavation continues the right upper section in 1.5 m increments, maintaining an offset from the face. Support is installed using shotcrete, steel frames, spacers, and tensioners, completing the structural cover and repeating the construction cycle.

3. Third stage: Benching of the left side core

The left core is excavated in 3 m increments and with a significant offset from the upper face. The gable end is stabilized with shotcrete, the steel frame elements are installed, and the structural support is completed.

4. Fourth stage: Benching of the right-side core

The right core is excavated, maintaining an offset from the left. The same support scheme is applied (shot concrete and metal frames) and, finally, the waterproofing systems and the final lining of the tunnel are installed.

For procedure ST2.

1. First stage: Upper half section

This stage begins with the installation of caissons and the construction of a tie beam at the portal. Subsequently, the upper half section is excavated in 2 m increments, stabilizing the ground with shotcrete and steel frames. The support is completed with additional layers of concrete, and the process is repeated cyclically until the caisson is finished.

2. Second stage: Central core benching

This stage consists of excavating the central core in increments of up to 4 m. This stage can be carried out in stages, once the excavation of the upper section of the entire tunnel is complete.

3. Third stage: Left side core benching

The left side is excavated in 3 m increments, maintaining an offset from the face. The wall is stabilized with shotcrete, steel frame elements are installed, and the support is completed with structural shotcrete.

4. Fourth stage: Benching of the right-side core

Similar to the left side, the right core is excavated with offset control. Shotcrete and steel frames are applied for support. Finally, waterproofing systems (geotextile and geomembrane) are installed, and the final tunnel lining is applied.

For procedure ST3:

1. First stage: Side sections of the upper half-section

The side sections are excavated in 2 m increments, compacting the soil, and applying a first layer of fibre-reinforced shotcrete to stabilize the arch.

2. Second stage: Central pillar of the upper half-section

The central core is excavated in 1 m increments, followed by support using shotcrete, installation of steel frames, spacers, and tensioners. Subsequently, the structural lining is completed, and the construction cycle is repeated.

3. Third stage: Benching of the central core

This consists of excavating the central core of the bench, which can be carried out once the excavation of the upper half-section is complete throughout the tunnel.

4. Fourth stage: Benching of side cores (left and right)

The side cores are excavated, maintaining offsets with respect to the face. The walls are stabilized with shotcrete and metal frames. Finally, the waterproofing systems (geotextile and geomembrane) are installed, and the tunnel's final lining is applied.

To model the shotcrete, the time-dependent strength gain was simulated, considering a daily excavation advance. Figure 13 shows the shotcrete strength development curve as a function of setting time that was adopted in the simulation. It should be noted that this curve was initially used

 doi:10.20944/preprints202605.0471.v1

in the model as a preliminary assumption; however, the behaviour was subsequently adjusted based on test results obtained from the shotcrete mixtures used at the site.

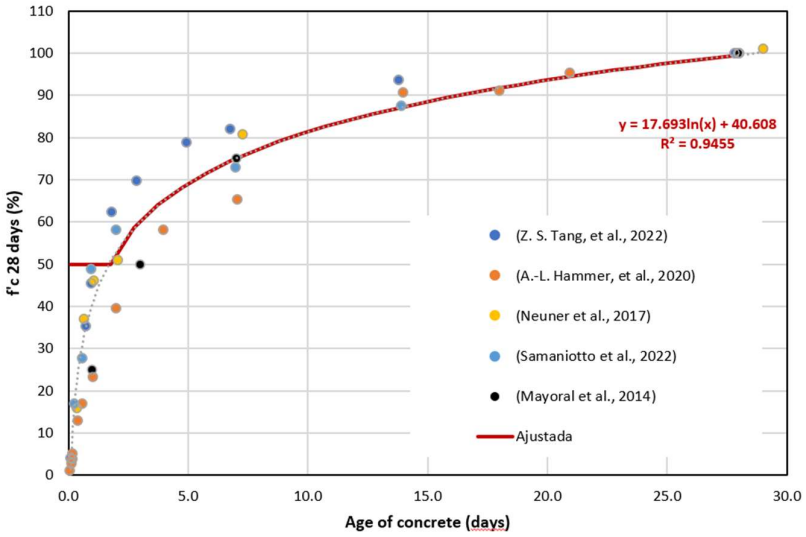

Figure 13. Strength curve with respect to setting time of shotcrete using the Concrete Hardening Law.

Figure 14, 15 and 16 also shows a view of the structural elements used in the numerical model. Furthermore, the soil behaviour was considered using the Mohr-Coulomb failure criterion.

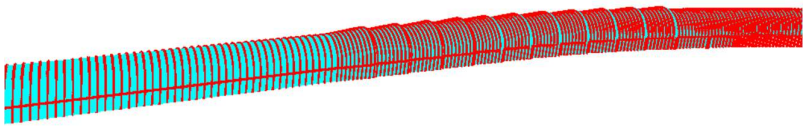

Figure 14. BEAM-type structural elements in red used to simulate the metal frames of the tunnel.

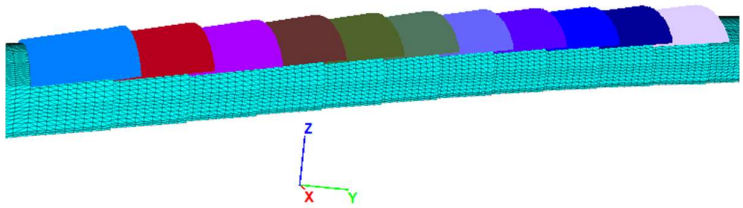

Figure 15. PILE-type structural elements used to simulate the tunnel alignments.

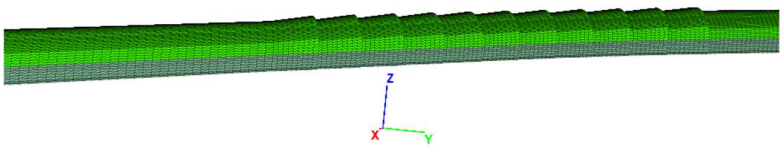

Figure 16. SHELL-type structural elements used to simulate the shotcrete of the tunnel.

To evaluate the stability of the shotcrete, fore poling elements, and steel frames, interaction diagrams—also known as capacity limit curves (CLC)—were used. In contrast, the stability of CABLE-type elements was verified by comparison with the allowable tensile force of the element.

 doi:10.20944/preprints202605.0471.v1

5. Tunneling Simulation Results

5.1. Displacements

Ground displacements were first evaluated under dry conditions. At the end of excavation, maximum displacements of about 3.26 cm were calculated at the tunnel crown, particularly within the Geotechnical Unit 2. These displacements result from stress release during excavation in a zone of lower stiffness. Figure 17 shows the distribution of the displacement obtained at the end of the tunneling simulation.

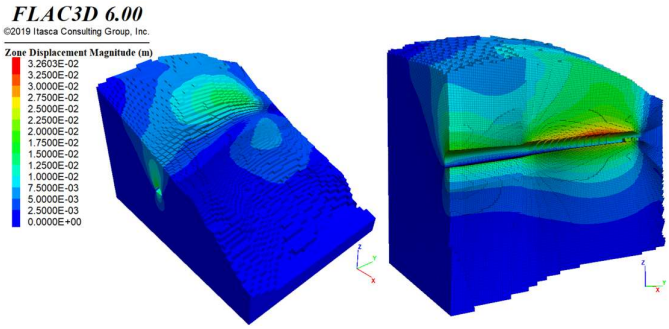

Figure 17. Overview of total displacements at the end of the tunnel construction, along the tunnel alignment. Units in [m].

5.2. Safety Factors

Safety factors were calculated at intermediate construction stages to evaluate tunnel face and surrounding stability. The capacity-to-demand criterion proposed by Mayoral (2014) was used to determine the factor of safety, and is expressed as follows:

$$FS = \frac{\tau_{cap}}{\tau_{act}} \tag{9}$$

where:

$$\begin{aligned} \tau_{cap} &= c + p' \tan \varphi \\ \tau_{act} &= \frac{1}{3}\sqrt{(\sigma_1 - \sigma_2)^2 + (\sigma_2 - \sigma_3)^2 + (\sigma_1 - \sigma_3)^2} \\ p' &= (\sigma_1 + \sigma_2 + \sigma_3)/3 \\ \sigma_1, \sigma_2, \sigma_3 &= \textit{Main efforts} \end{aligned}$$

Figure 18 shows the results at three different intermediate steps, where the safety factors result critical at the tunnel face.

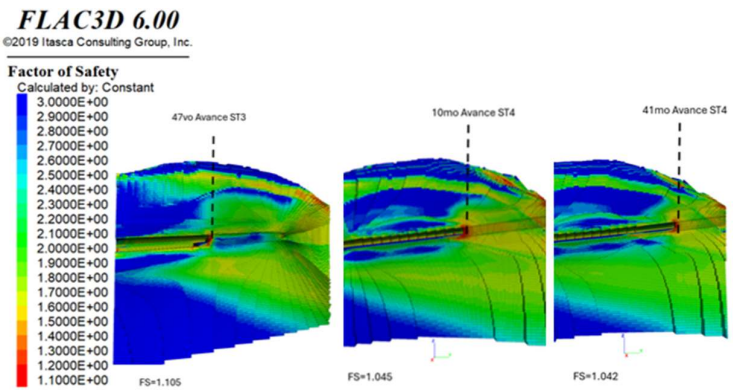

Figure 18. Safety factor contours during the construction process.

 doi:10.20944/preprints202605.0471.v1

FS values around 1.6 indicate adequate global stability of the excavation. However, lower values close to 1.1 occur at the tunnel face during all construction stages, representing the most critical condition. Despite this, no global failure mechanism develops above the crown, suggesting that any instability would likely be limited to local spalling or minor detachments at the tunnel face. In conclusion, the tunneling process will not impact on the global stability of the slope, as can be seen in the displacements and safety factor contours.

6. Seismic Slope-Tunnel Performance Evaluation

Finally, the seismic evaluation was made for the tunnel-slope system, considering as initial condition the output of the tunnelling simulation under monotonic loading, to adequately represent the stress and strain states.

For underground structures with circular or semi-circular cross-sections, many standards use the diameter strain ratio as an evaluation index, defined as the ratio of convergence, ΔD, to the original diameter D:

$$\frac{\Delta D}{D} = \frac{\gamma_{max}}{2} \tag{10}$$

As defined in Equation (1) diameter strain ratio can be calculated in function of the maximum distortion of the tunnel ◎max, which can be obtained from unidimensional propagation analyses, when the tunnel stiffness is similar to that of the soil. Nevertheless, for a more accurate approximation, the effects of soil-structure interaction should be considered.

Eurocode 8 establishes limits of 0.5% for tunnels in rock and between 1% and 2% for tunnels in soil, while FHWA, suggests values of 1% for cast-in-place concrete linings and 2% for segmental linings. Regarding the longitudinal behavior the maximum axial force reached during the earthquake mustn't exceed the lining structural capacity.

Site response analyses were conducted to verify the seismic demand on the tunnel support system. Three geotechnical units were defined based on the geological model, with shear wave velocities assigned from geophysical data (Table 5). Due to the lack of dynamic laboratory tests, shear modulus degradation (G/Gmax) and damping ratio (λ) curves were adopted from the literature according to material type. Figure 19 show the curves used.

Table 5. Dynamic properties of geotechnical units.

Unit	γ (ton/m3)	ν	Vs (m/s)
Slope deposits	2.0	0.35	250-400
Highly weathered shales and limestones	2.4	0.3	400-600
Moderately weathered shales and limestones	2.4	0.3	600-800

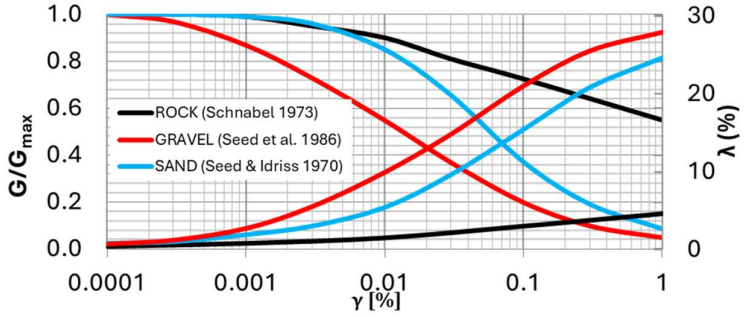

Figure 19. Shear stiffness degradation, G/Gmax, and damping ratio curves, λ.

 doi:10.20944/preprints202605.0471.v1

The seismic environment was defined using the deterministic approach, and ground motion prediction models (García, 2006; Jaimes and García-Soto, 2020) were used, which were calibrated with records from a rock-site station near the studied site, verifying that the spectral form were similar.

Two different types of seismic sources were considered in the analyses, intraplate and interface events. In the case of the intraplate earthquake attenuation models showed reasonable agreement, but they underestimated pseudo-acceleration at some periods in comparison to the seismic record that generates the maximum accelerations in the reference station; therefore, the seismic record was used directly as input motion. This corresponds to Mw=8.2 Pijijiapan (Chiapas) intraplate earthquake. For the maximum interplate scenario (Mw 8.6), PGA was estimated using attenuation model of García (2006), and the Crucecita (Oaxaca) record was scaled accordingly, as it represents the largest interplate PGA recorded near the potential rupture zone. The resulted response spectra are shown on Figure 20. Finally, the input motions applied at the base of the model was defined trough deconvolution with the program SHAKE (Schnabel et al. 1972) and applied as a stress time history according to the compliant base approach (Itasca, 2019). Only the results corresponding to scaled interplate event are shown in this paper due to it generates the greatest seismic motions.

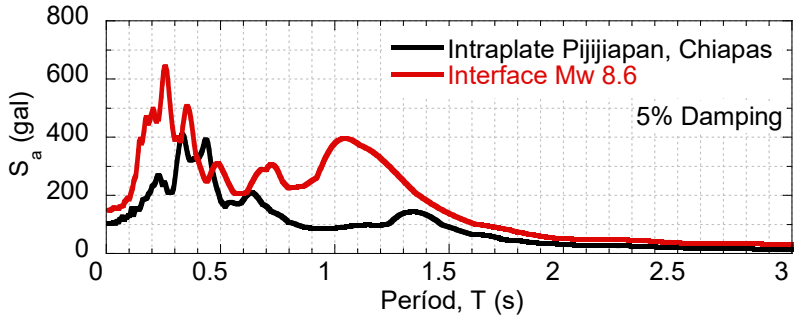

Figure 20. Response spectra of earthquakes considered.

7. Results of Dynamic Analysis

7.1. Ground Stability During the Earthquake

Simulations of the tunnel's seismic response were performed using three-dimensional finite difference models of the critical zones. These simulations were conducted after the completion of the final tunnel lining stages, as part of the construction process simulation, to accurately represent the stress and strain fields around the lining.

To monitor the behavior of the ground and the tunnel in terms of displacements during the earthquake simulation, control points were placed in three sections: the left portal, at the central section and of the right portal. Figure 21 shows the location of these points in the model.

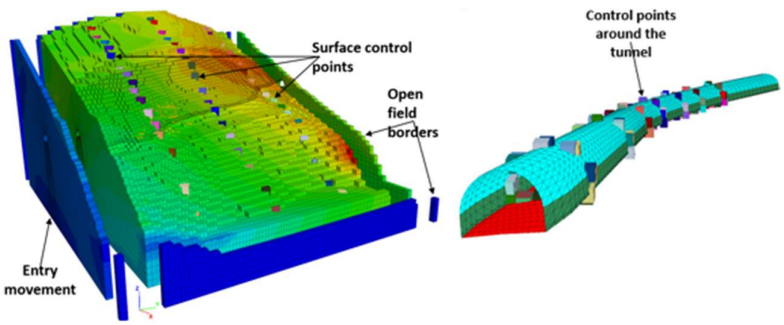

Figure 21. Finite difference mesh, with the boundary conditions and the control points location.

 doi:10.20944/preprints202605.0471.v1

The displacement histories at the slope surface are depicted in Figure 22, showing that all monitored sections exhibit permanent displacements following the earthquake. This behavior indicates accumulation of plastic deformation within the slope mass (Bray and Travasarou, 2007). From all the sections, that located at the right tunnel presents the greatest accumulated displacements, reaching values up to 70 cm. This can be associated with the proximity of the tunnel to the failure surface, which affect the slope stability due to shear stress concentrations during construction, and confining stress reductions. Given the pre-existing instability of the slope, the occurrence of large irreversible displacements of this magnitude under seismic loading suggests that the slope is susceptible to progressive failure following the earthquake.

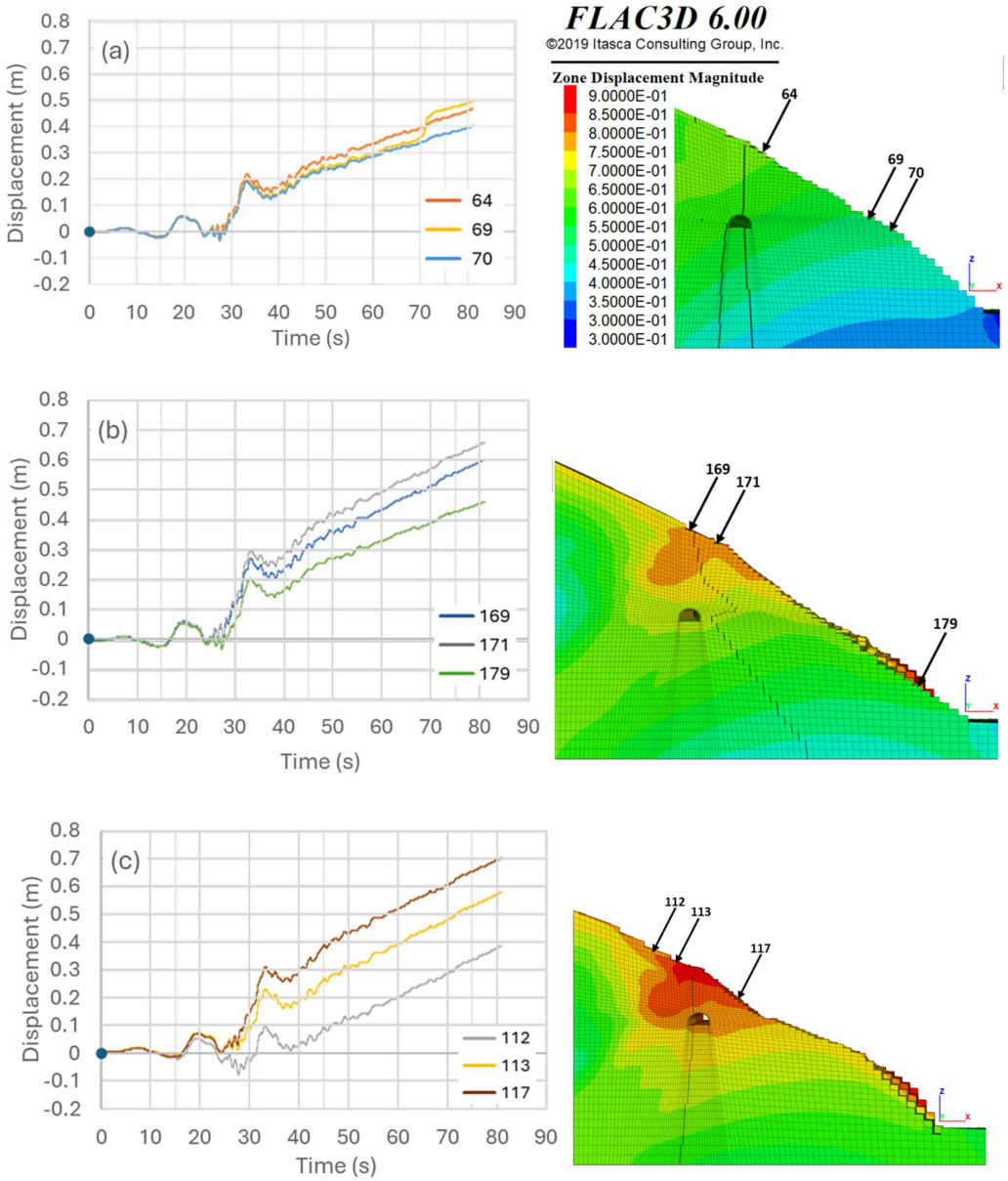

Figure 22. Slope displacement histories (a) at the left tunnel portal, (b) at the central section, and (c) at the right tunnel portal. Units in [m].

 doi:10.20944/preprints202605.0471.v1

7.2. Lining Performance During the Earthquake

To assess the structural performance of the tunnel under seismic loading, relative displacements around the lining were obtained. For deformation in the tunnel cross-section, distortions, γ_max, and normalized convergences, ΔD/D, were calculated, and for axial and curvature deformations along tunnel longitudinal axis, maximum axial force reached during the earthquake was calculated. Figure 18 shows the corresponding results at the same cross-sections used for the slope displacement analysis. Points 1 and 2 from Figure 18 were used for the estimation of γ_max, and points 3 and 4 for ΔD/D. The results indicate that the largest seismic demand occurs at the central section, and the right tunnel portal, consistent with the zones of largest slope seismic displacements. However, these conditions do not significantly represent an instability condition for the tunnel cross section, due to maximum ΔD/D was approximately 0.15%, which is lower than the limit of 0.5% recommended by the Eurocode for underground structures in rock.

In the case of the longitudinal axis, maximum axial force of ≈ 10 MN is reached during the earthquake. This value is presented on the left wall of the lining, in the zone of maximum curvature of the tunnel. This result agreed with the seismic permanent displacements of the slope (Figure 23) due to between the right tunnel portal and the central section occurs the maximum relative displacements. Nevertheless, the estimated allowable axial force in the lining was 70 MN (considering the cross-section area of the left wall and the compressive strength of the concrete f'c=30 MPa), which is greater than the 10 MN reached during the earthquake. This result demonstrates that the tunnel lining can accommodate the expected seismic deformations without compromising its structural integrity, even under the slope instability conditions present at site.

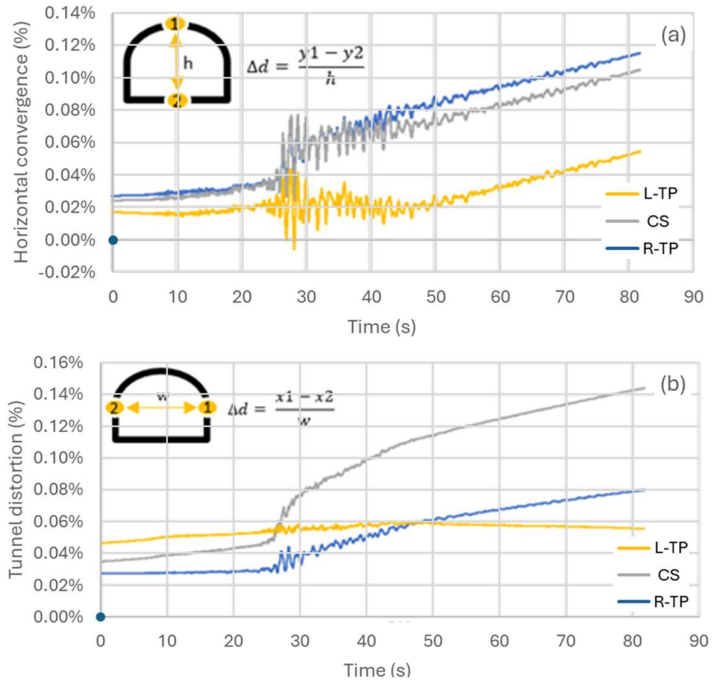

Figure 23. Resultant (a) distortions γ_{max}, and (b) horizontal convergences $\Delta D/D$ histories, at the left tunnel portal, L-TP, central section, CS, and right tunnel portal, R-TP.

The longitudinal structural response of the tunnel lining was evaluated in terms of axial forces, obtaining the tunnel deformation after the earthquake. Figure 24 shows these deformations, identifying the 3 different sections considered for comparison of results where:

1. In the most critical part of the slope – (RTP-CS)
2. Central part – (CS)
3. In the straight section of the entrance portal – (LTP-CS)

 doi:10.20944/preprints202605.0471.v1

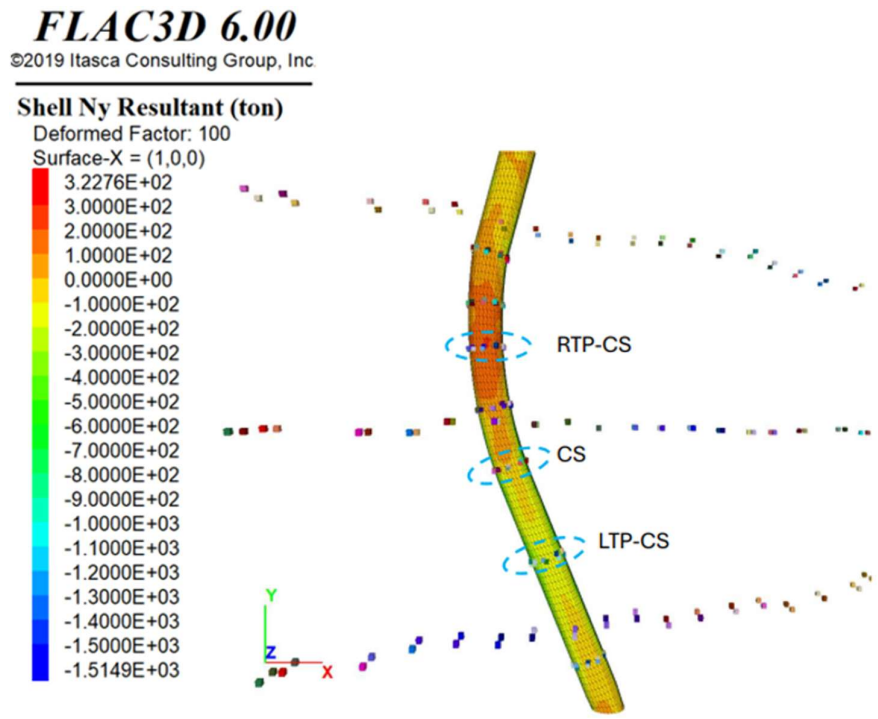

Figure 24. Axial force distribution and selected sections (RTP-CS, CS, LTP-CS) along the tunnel.

Figure 25 shows the tunnel displacement in plant view and Figure 26 shows the longitudinal displacement in both sides. The solid side indicates the deformation with a distorted scale of the mesh, and the thin side does not.

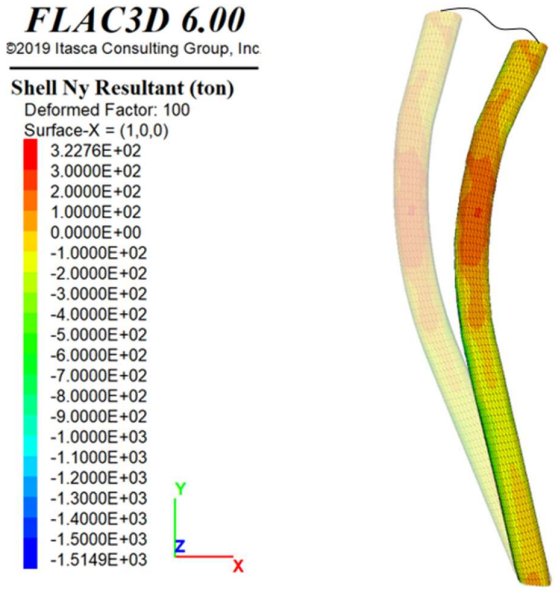

Figure 25. Plan view of axial stresses of the tunnel lining.

 doi:10.20944/preprints202605.0471.v1

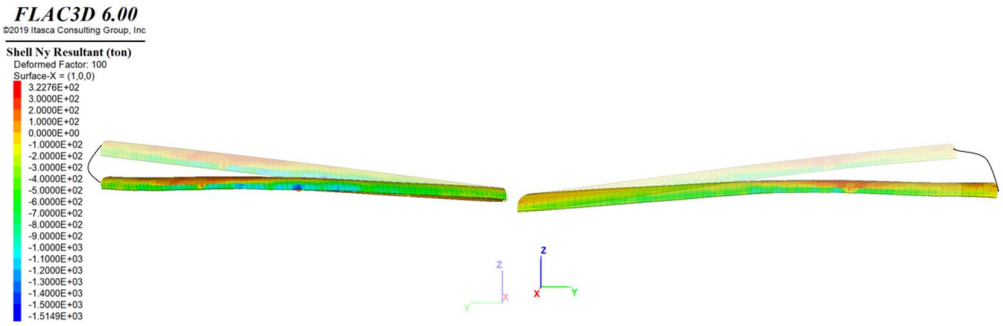

Figure 26. Longitudinal axial stresses of the tunnel lining.

The results show that the lining is predominantly subjected to compressive forces along its longitudinal axis, with maximum values reaching approximately -1.5×10^3 tons. This indicates that seismic loading induces a significant axial demand, especially in areas affected by the tunnel curvature and ground instability.

Figure 24 shows the distribution of longitudinal axial stresses in the tunnel lining. Negative values (green to blue tones) indicate that the lining is primarily subjected to compressive axial stresses along its longitudinal axis. Compression concentrations are mainly located in the CS and LTP-CS zones. On the other hand, areas with warm colors (yellow to red) represent regions with tensile axial stress. The spatial variation of colors along the tunnel demonstrates a non-uniform distribution of longitudinal loads, influenced by geometric conditions, seismic and ground deformation effects.

In the RTP-CS zone, compressive axial stresses are shown on the right side and tensile stresses on the left, due to the tunnel's curvature and its location in the most unstable area of the slope. Figure 27 shows the graphic of axial force distribution and time-history response at this section.

In the CS zone, a slight curvature of the tunnel axis and proximity to instability are shown, reflecting the influence of differential ground movement, with compressive values on the right side and tensile values on the left. Figure 28 shows the graphic of axial force distribution and time-history response at this section.

Finally, in the LTP-CS zone, only compression values are found because this is a straight section and is located far from the unstable zone. Figure 29 shows the graphic of axial force distribution and time-history response at this section.

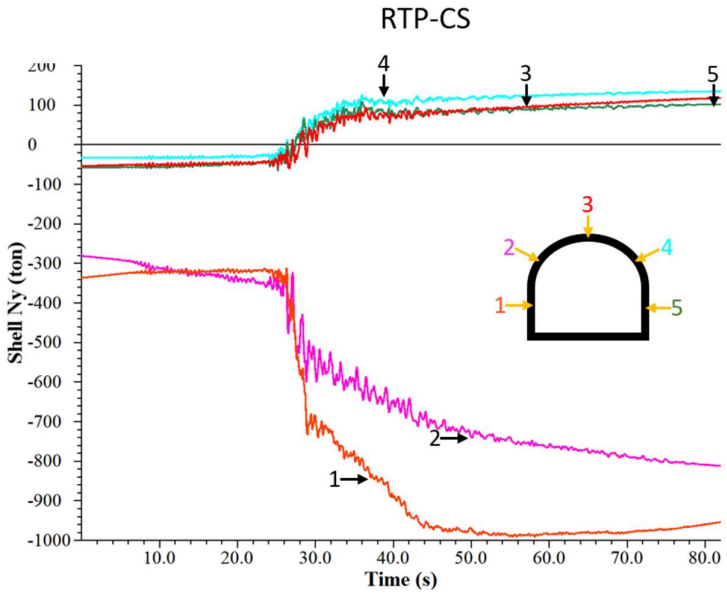

Figure 27. Axial force distribution and time-history response at RTP-CS section.

 doi:10.20944/preprints202605.0471.v1

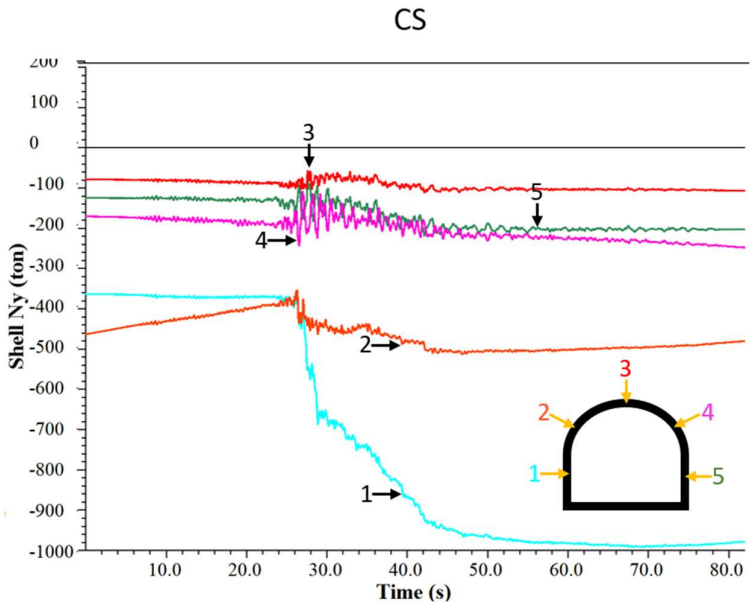

Figure 28. Axial force distribution and time-history response at CS section.

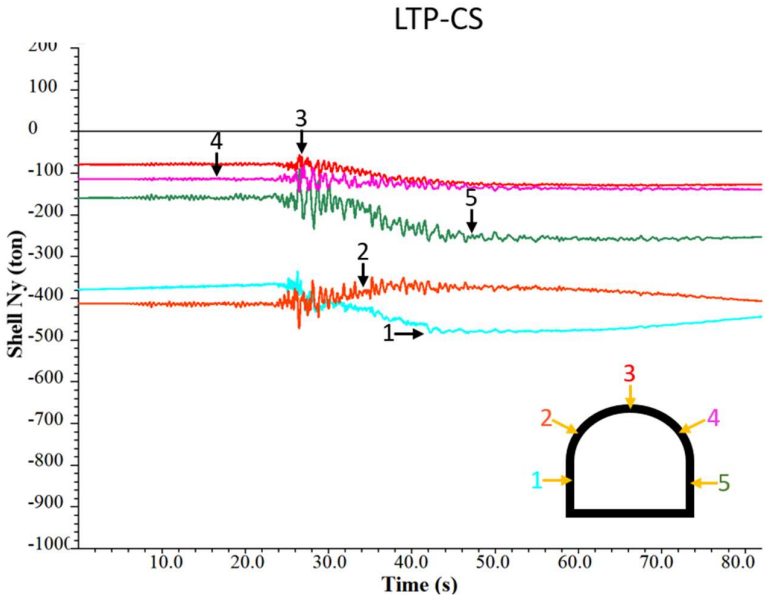

Figure 29. Axial force distribution and time-history response LTP-CS section.

The time response indicates that maximum compressive forces develop during the phase of greatest seismic intensity, with clear peaks observed between approximately 30 and 50 seconds. This behavior remains constant in all cases, although the amplitude of the response varies, highlighting the influence of the aforementioned factors.

For the three sections previously evaluated (RTP-CS, CS and LTP-CS), 3 tributary areas were defined in order to estimate the longitudinal stresses in each section and subsequently compare them with the concrete strength to assess structural safety. The reinforcement layout and the divisions adopted to define the tributary areas are shown in Figure 30.

 doi:10.20944/preprints202605.0471.v1

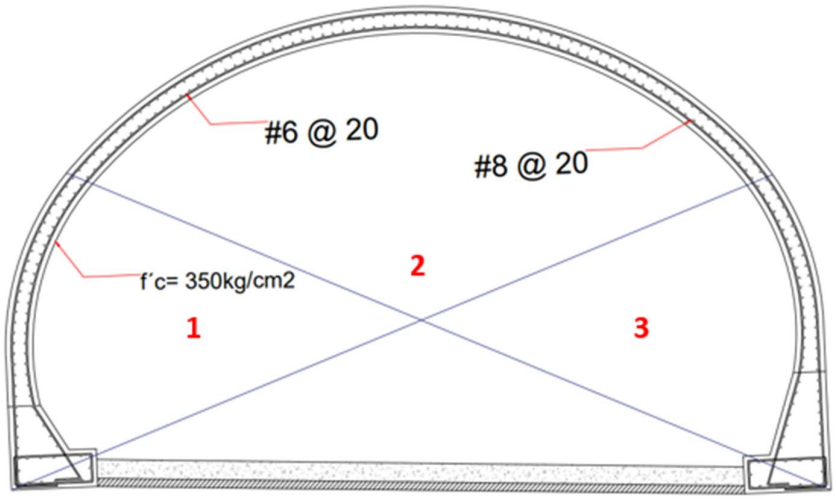

Figure 30. Reinforcement layout with the divisions for the tributary areas.

Using the previously defined control points (Figure 31), the maximum stresses in the concrete were obtained for each section. The results indicate that, at all control points, the computed stresses remain below the concrete compressive strength of 350 kg/cm².

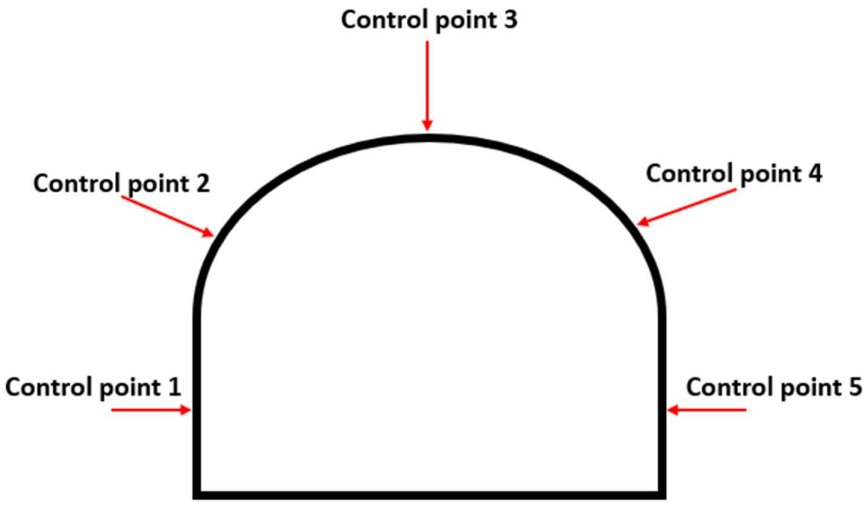

Figure 31. Control points defined.

In the RTP-CS section, two values indicate compressive stresses on the left side of the tunnel, while the remaining three values correspond to tensile stresses on the right side. As discussed previously, this behavior is consistent with the curvature of this section and its proximity to the slope failure zone.

 doi:10.20944/preprints202605.0471.v1

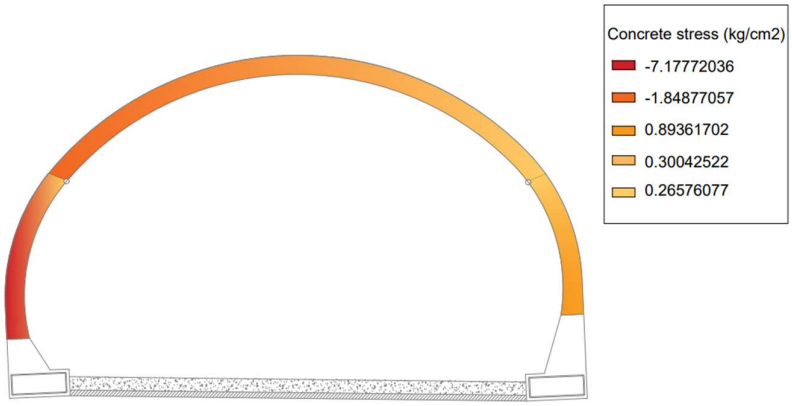

Figure 32. Concrete stress of section RTP-CS.

In contrast, for the CS and LTP-CS sections, all obtained values indicate tensile stresses across the evaluated areas. The maximum value, equal to −27.3, is observed in the LTP-CS section, which is located along the straight section of the tunnel and at a greater distance from the slope failure zone.

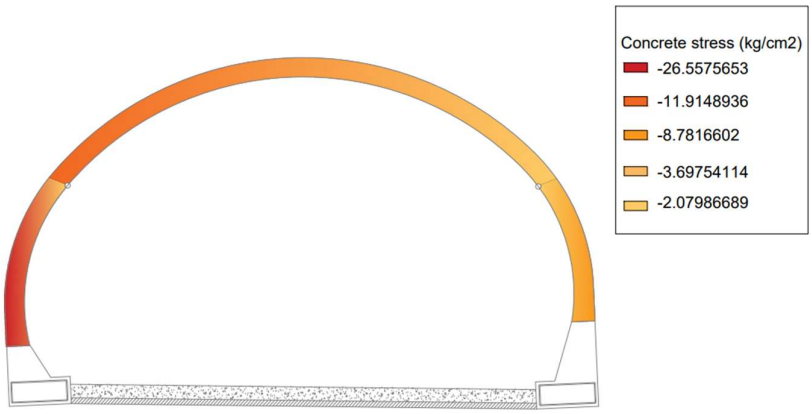

Figure 33. Concrete stress of section CS.

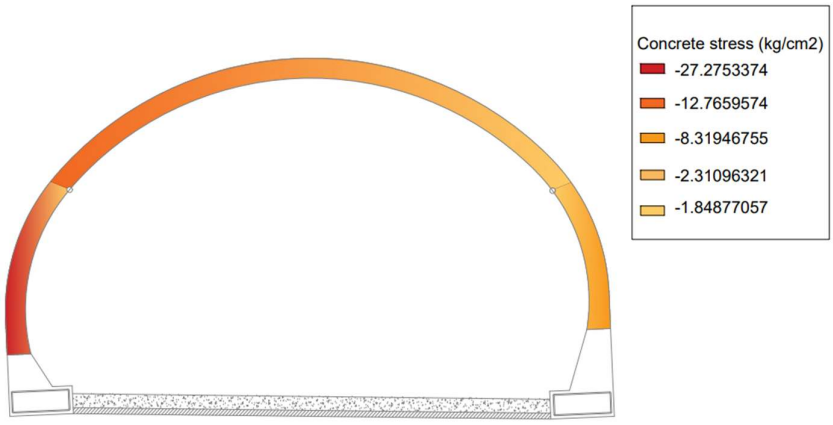

Figure 34. Concrete stress of section LTP-CS.

8. Conclusions

The observed slope failure was successfully reproduced through back-analysis using strength reduction methods, allowing the calibration of representative geomechanical parameters for the rock

 doi:10.20944/preprints202605.0471.v1

mass under near-critical stability conditions. Three-dimensional numerical simulations of tunnel excavation indicate moderate ground deformations, with maximum displacements of approximately 3.3 cm at the tunnel crown, mainly associated with stress release during excavation in zones of reduced stiffness. The stability analyses during construction stages show global safety factors close to 1.6, indicating adequate stability of the excavation. The most critical condition occurs at the tunnel face, where safety factors approach 1.1, suggesting the possibility of localized instabilities such as minor spalling or small detachments. The seismic response of the tunnel lining shows maximum diametral strains of approximately 0.15%, which are well below the limits recommended by international design standards for underground structures, confirming the structural adequacy of the lining under seismic loading. Regarding the tunnel influence on the slope stability the greatest accumulated displacement match with the section where the tunnel is closer. Overall, the proposed tunnel solution represents an effective mitigation measure to bypass unstable slopes and maintain roadway functionality, demonstrating satisfactory performance under both static and seismic loading conditions in complex geological environments. A clear spatial variability in the axial force distribution was identified along the tunnel. The RTP-CS section, located in the most critical part of the slope, exhibits a combined tension–compression behavior across the cross-section, which is attributed to tunnel curvature and its proximity to the unstable slope. The CS section shows a similar but less pronounced trend, whereas the LTP-CS section, located in a straight section of the tunnel and farther from instability effects, is characterized by a more uniform compressive response. The time-history analysis indicates that maximum axial forces occur during the strong-motion phase of the seismic event, approximately between 30 and 50 seconds. This behavior is consistent across all sections, although the amplitude of the response varies depending on local geometric and geotechnical conditions. From a structural safety perspective, the stress evaluation based on tributary areas shows that all computed stresses remain below the concrete compressive strength of 350 kg/cm², demonstrating that the tunnel lining maintains an adequate safety margin under the analyzed seismic scenario. Overall, these results highlight the importance of considering soil–structure interaction, tunnel geometry, and proximity to unstable zones in the seismic assessment of underground structures, as sections with curvature and located near slope instability zones are more susceptible to differential stress distributions.

Author Contributions: Conceptualization, Juan Manuel Mayoral, Paola Martínez Castelán and Azucena Román de la Sancha; Methodology, Juan Manuel Mayoral, Paola Martínez Castelán and Azucena Román de la Sancha; Software, Paola Martínez Castelán and Mauricio Peréz; Validation, Mauricio Peréz; Formal analysis, Paola Martínez Castelán and Mauricio Peréz; Investigation, Juan Manuel Mayoral, Paola Martínez Castelán and Mauricio Peréz; Resources, Francisco Suarez Fino; Data curation, Francisco Suarez Fino; Writing – original draft, Paola Martínez Castelán; Writing – review & editing, Juan Manuel Mayoral, Mauricio Peréz, Azucena Román de la Sancha and Francisco Suarez Fino; Supervision, Juan Manuel Mayoral. All authors have read and agreed to the published version of the manuscript.

Funding: This research received no external funding.

Institutional Review Board Statement: Not applicable.

Informed Consent Statement: Not applicable.

Data Availability Statement: The original contributions presented in this study are included in the article. Further inquiries can be directed to the corresponding author(s).

Conflicts of Interest: The authors declare no conflict of interest.

References

1. Bray, J.D.; Travasarou, T. Simplified procedure for estimating earthquake-induced deviatoric slope displacements. *J. Geotech. Geoenviron. Eng.* 2007.
2. CEN. *EN 1998-4 Eurocode 8: Design of Structures for Earthquake Resistance – Part 4: Silos, Tanks, and Pipelines*; European Committee for Standardisation: Brussels, Belgium, 2006.

 doi:10.20944/preprints202605.0471.v1

3. Chen, Y.; Li, S.; Sun, Z.; Liu, P.; Zhang, S. Deformation mechanism and control technology of tunnel–landslide interaction based on numerical simulation. *Appl. Sci.* 2024, 14, 5479.
4. Cheshomi, A.; Ahmadi, M. Interaction between tunnel excavation and slope stability using numerical modeling. *Geotech. Geol. Eng.* 2013.
5. Ferrario, M.F.; Livio, F. Rapid mapping of landslides induced by heavy rainfall in the Emilia-Romagna (Italy) region in May 2023. *Remote Sens.* 2024, 16, 122.
6. FHWA. *Technical Manual for Design and Construction of Road Tunnels – Civil Elements*; Publication No. FHWA-NHI-10-034; Federal Highway Administration: Washington, DC, USA, 2009.
7. Hoek, E.; Brown, E.T. The Hoek–Brown failure criterion and GSI – 2018 edition. *J. Rock Mech. Geotech. Eng.* 2019, 11, 445–463.
8. Jaimes, M.A.; García-Soto, A.D. Updated ground motion prediction model for Mexican intermediate-depth intraslab earthquakes including V/H ratios. *Earthq. Spectra* 2020, 36, 1298–1330.
9. Li, Z.; Li, J.; Li, W. Evaluation of seismic response of tunnels near slope surfaces and performance of anti-seismic measures. *Soil Dyn. Earthq. Eng.* 2023, 165, 107734.
10. Mayoral, J.M.; Melis-Maynar, M.J.; Roman, A. Integral approach of performance-based design for tunnels. *Transp. Res. Rec.* 2015, 2522.
11. Mayoral, J.M. Performance evaluation of tunnels built in rigid soils. *Tunn. Undergr. Space Technol.* 2014, 43, 1–10.
12. Mitoulis, S.A.; Argyroudis, S.A.; Winter, M.G. Vulnerability of transport infrastructure to landslides and implications for resilience. *Transp. Geotech.* 2021, 28, 100525.
13. Sarah, D.; Zulfahmi, Z.; Putra, M.H.Z.; Madiutomo, N.; Gunawan; Ahmid, D.A. Back analysis of rainfall-induced landslide in Cimanggung District of Sumedang Regency in West Java using deterministic and probabilistic analyses. *Geosciences* 2024, 14, 347.
14. Vracevic, N.; Marinković, N.; Orešković, J. Comparison of measured and calculated interactions between slope creeping and tunnel structures. *CE/Papers* 2019, 2, 505–510.
15. Wei, H. A case study in Fengjie County, Chongqing, China, July 2, 2016. In *Proceedings of ASCE Conference Papers*, 2025.
16. Wu, D.; Chen, X.; Tao, Y.; Meng, X. Estimating Mohr–Coulomb strength parameters from the Hoek–Brown criterion for rock slopes undergoing earthquake. *Sustainability* 2023, 15, 5405.
17. Power, M.; Fishman, K.; Richards, R.; Makdisi, F.; Musser, S.; Youd, T.L. *Seismic Retrofitting Manual for Highway Structures: Part 2 – Retaining Structures, Slopes, Tunnels, Culverts, and Roadways*; Report No. FHWA-HRT-05-067; Federal Highway Administration (FHWA), U.S. Department of Transportation: McLean, VA, USA, 2004.